Desalination and Water Treatment
www.deswater.com

doi: 10.5004/dwt.2021.26994

217 (2021) 1–21
March

Parametric study and multi-objective optimization of a combined cooling, desalination and power system

Shihe Zhou[a,*], Xinyu Liu[a], Yin Feng[b], Yongning Bian[a,*], Shengqiang Shen[c,*]

[a]*School of Ocean Science and Technology, Dalian University of Technology, Panjin 124221, Liaoning, China, emails: zhoushihe@dlut.edu.cn (S. Zhou), ybian@dlut.edu.cn (Y. Bian), liuxinyu1996@mail.dlut.edu.cn (X. Liu)*
[b]*Dalian Chenggao Technologies Co., Ltd., Dalian 116024, Liaoning, China, email: 407506049@qq.com*
[c]*School of Energy and Power Engineering, Dalian University of Technology, Dalian 116024, Liaoning, China, email: zzbshen@dlut.edu.cn*

Received 22 May 2020; Accepted 24 December 2020

ABSTRACT

Multi-generation system driven by alternative energies provides a promising solution for meeting the challenges of energy and fresh water with the rapid development of economy. In this paper, an innovative combined cooling, desalination and power (CCDP) cycle is proposed, which integrates multi-effect distillation (MED) and ejector refrigeration cycle with organic Rankine cycle. The surface warm seawater further heated by the solar energy and the deep cold seawater are taken as the heating and cooling sources, respectively. Mathematical model of the combined cycle is developed to evaluate the thermodynamic and economic performances. The effects of generation temperature, condensing temperature and evaporating temperature are investigated, and comparative analysis of five working fluids is conducted as well. The results indicate that the CCDP system with lower condensing temperature and generation temperature is conducive to obtaining higher exergy efficiency η_{ex}, but leads to the increase of total cost rate (TCR). Furthermore, for the trade-off between thermodynamic and economic performances, a multi-objective optimization is conducted in terms of η_{ex} and TCR as objective functions. The Pareto optimal solutions (POS) for the five working fluids are determined based on a fast and elitist non-dominated sorting genetic algorithm (NSGA-II) and decision-making technique. According to the results of POS, R601 has the best performance with 6.51×10^4 \$/y of TCR and 31.62% of exergy efficiency, followed by R245fa, R600a, R236ea and R152a. The percentage of initial investment and the distribution of exergy flow for the POS of R601 are obtained as well.

Keywords: Combined cooling; Desalination and power system; Organic Rankine cycle; Multi-effect distillation; Ejector refrigeration; Ocean thermal energy; Multi-objective optimization

1. Introduction

With the population explosion and the rapid development of economy, energy and fresh water have become the two greatest challenges of the 21st century [1]. Seawater desalination has been proved to be an effective means to alleviate the shortage of fresh water resources. It is of great practical significance for the coastal regions to make full use of the geographical advantage to develop desalination industry. Currently, the available desalination technologies are mainly categorized into thermal (phase change) and membrane (non-phase change) processes. However, as an energy-intensive industry, the high energy consumption of desalination has become the main bottleneck restricting its promotion and application. The specific energy consumption of thermal desalination, such as multi-stage flash (MSF)

* Corresponding authors.

1944-3994/1944-3986

and multi-effect distillation (MED), is up to 20–27 and 14–21 kWh/m^3[2], respectively. Even the most widely used membrane process, namely reverse osmosis (RO), has a specific energy consumption of 3–4 kWh/m^3 [3]. Meanwhile, as the environmental problem is worsening due to the use of fossil fuel, the low-grade waste heat and alternative energy have been paid more and more attentions for improving the energy utilization efficiency and reducing pollution. Therefore, the process integration with desalination for energy saving and environment friendly has a promising development prospect [2].

The thermal desalination processes, such as MSF, MED, humidification and dehumidification (HDH) [4] and spray flash evaporation [5,6], usually have lower operating temperature and thus are attractive in the field of low-grade thermal energy utilization. Various configurations of system integration have been emerging, and the corresponding researches have been focusing on the performance study and parametric analysis of the novel system. Chen et al. [7] performed a thermodynamic analysis on the multi-stage spray flash desalination system, and the result found that the energetic efficiency can be promoted at higher numbers of operating stages. Moreover, Chen et al. [8] also integrated the ejector with the multi-stage spray-assisted desalination system in order to match the high-temperature heat source, and the production ratio was found to be greatly improved by 35%. Al-Weshahi et al. [9] developed a combined desalination and power system, where the generated vapor in each stage of MSF is extracted as the heat source of organic Rankine cycle (ORC). The results indicated that higher evaporating temperature and lower cooling water temperature are beneficial for getting higher exergy efficiency. Baccioli et al. [10] analyzed the thermal and economic performances of the cogeneration system integrating MED with ORC. Results showed that the second law efficiency can be improved especially at smaller scale of the distillate production, and the integration with ORC also cuts down the payback time in most cases. Aguilar-Jiménez et al. [11] investigated the thermal performance of ORC-MED system driven by waste heat. The results showed that the system integration contributes to the improvement of energy efficiency and fresh water production while only requiring a small increase in heat transfer area. Calise et al. [12] analyzed the economic performance of a combined cooling, heating and power (CCHP), and desalination system under different time bases, which is driven by solar and geothermal energy. The subsystems of generation, refrigeration and desalination adopted ORC, absorption chiller and MED, respectively. The results indicated that the proposed system has high efficiency and flexibility, and the capital cost should deserve sufficient considerations for the optimization of design and operation. You et al. [13] also proposed a CCHP and desalination system with a gas turbine as the prime mover, which includes ORC, ejection refrigeration cycle (ERC) and MED. Performance analysis revealed that the exergy and overall energy efficiencies of the proposed system can reach 41.26% and 46.70%, respectively. He et al. [14] investigated a novel HDH-ORC cycle where the extracted vapor from turbine is used to further heat the seawater from the dehumidifier. They found that the extraction ratio of turbine has the opposite impacts on the power output and fresh water production.

In addition, as one of the renewable energies, ocean thermal energy is a kind of solar energy collected in the form of the temperature difference between the deep cold seawater and the surface warm seawater. Due to the characteristics of large reserves and stability, ocean thermal energy is expected to provide energy supply for low latitudes. Nowadays, the ocean thermal energy conversion (OTEC) cycle has been divided into three main types: open, closed and hybrid. However, due to the small available temperature difference, even the most efficient closed cycle has an energy efficiency of less than 5% [15]. For further improving the efficiency of energy utilization of OTEC, the previous studies have been carried out mainly focusing on the optimal selection of working fluid [16], improvement of cycle configuration [17], enhancement of available temperature difference [18] and system integration based on the energy cascade principle [19]. Compared with the ORC-based OTEC system, the Kalina, Uehara and GUO HAI cycles have been proved to be more efficient taking the ammonia-water mixture as working fluid, but the cycle configurations are more complex and the corresponding investment cost gets higher. Moreover, the solar-assisted OTEC cycle shows the potential to improve the thermal efficiency by enhancing the temperature difference between the heat sources [20]. In addition to the improvement of OTEC itself, it is also an attractive way to establish a multi-generation system based on the process integration method. Both Yuan et al. [19] and Bian et al. [21] conducted performance analysis of the solar-assisted hybrid OTEC system based on the Kalina cycle and ERC. The results indicated that the proposed systems can obtain higher energy efficiency than the separate Kalina cycle.

It should be noted that for the multi-generation system, while the thermodynamic performance is greatly improved, the economic performance must be considered as well in order to evaluate the economic feasibility of the system. Therefore, the multi-objective optimization of multi-generation system is quite necessary for the trade-off between thermodynamic and economic performances. Ahmadi et al. [22] conducted the multi-objective optimization of exergy and exergoeconomic performances for a combined power, cooling, fresh water and hydrogen system based on solar-assisted OTEC technology. Alirahmi et al. [23] carried out the multi-objective optimization of multi-generation system driven by geothermal and solar energy, which included an ORC cycle, a polymer electrolysis membrane electrolyzer, an absorption chiller, and an RO desalination unit. The objective functions were minimizing the total cost rate (TCR) and maximizing the exergy efficiency, and the non-dominated sorting genetic algorithm (NSGA-II) was adopted to obtain the Pareto optimal solution (POS) set. Rostamzadeh et al. [24] presented a comparative study of two combined cooling, heating and power (CCHP) systems, which took the ORC and Kalina cycle as the top cycle, respectively. The cooling and heating subsystems were ERC and vapor compression heat pump. The multi-objective optimization results indicated that the Kalina-based CCHP system has higher optimal thermal efficiency and total unit cost of product.

It can be found from the literature review that the multi-generation system driven by alternative energy provides a promising solution for improving energy efficiency and reducing energy consumption of desalination and greenhouse gas emissions. Therefore, facing the actual demand of remote islands at low latitudes, a novel combined cooling, desalination and power (CCDP) system integrating ORC-based OTEC cycle with ERC and MED is proposed in this study, which has not been reported yet in the previous researches to the best of our knowledge. The contributions of the present study are identifying the effects of design parameters and various working fluids on the thermodynamic and economic performances of the proposed CCDP system, and conducting multi-objective optimization study based on NSGA-II for determining the optimal design solution. The rest of this paper is organized as follows:

- The configuration of the proposed CCDP system will be described in section 2.
- Thermodynamic, economic and optimization models adopted in this study will be provided in section 3.
- In section 4, parametric study will be carried out to investigate the effects of key design parameters on performances of the proposed system with five working fluids. Furthermore, the multi-objective optimization in terms of the TCR and exergy efficiency will be conducted, and the Pareto optimal frontier for five working fluids and the corresponding optimal design solutions will be determined.
- The conclusions will be drawn in section 5.

2. System description

Schematic diagram of the proposed CCDP system is illustrated in Fig. 1, and the corresponding T-s diagram using dry working fluid is plotted in Fig. 2. The CCDP cycle is composed of generator, turbine, MED, ejector, evaporator, condenser, throttle valve, mixer and working fluid pumps. According to the previous research on the advantageous effect of solar assisting [18], it is assumed that the surface warm seawater goes through a solar-assisted module before entering the generator, and its temperature is raised to T_{14} (state point 14). In the present work, the temperature and mass flow rate of surface warm seawater at state point 14 keep constant, and thus the control volume in the chain-dotted line is selected to investigate the effects of design parameters and various working fluids for simplifying the simulation. In the generator, the working fluid is heated by the warm seawater and then gets to the state of superheated vapor (state point 3). Whereafter, the superheated vapor expands in the turbine, and a portion of it (state point 12) is extracted to the condenser I, namely the first effect of MED. The remaining expands to the state point 4 and then enters the ejector as the motive steam. In the ejector, the lower pressure vapor from the evaporator (state point 9) is extracted and mixed with the motive steam. Afterwards, the discharged vapor of the ejector (state point 5) flows into the condenser II, where it is condensed by the deep cold seawater. A part of the condensate (state point 7) returns the evaporator via an expansion valve, and the rest (state point 10) is pumped to the mixer, where it is mixed with the working fluid from the condenser I (state point 13). Finally, the working fluid is delivered back to the generator.

As displayed in Fig. 3, the MED desalination system mainly comprises horizontal-tube falling-film evaporators, flashing boxes of distillate and an end condenser. In addition, vacuum system is needed because the top brine temperature of MED is no more than 70°C. The

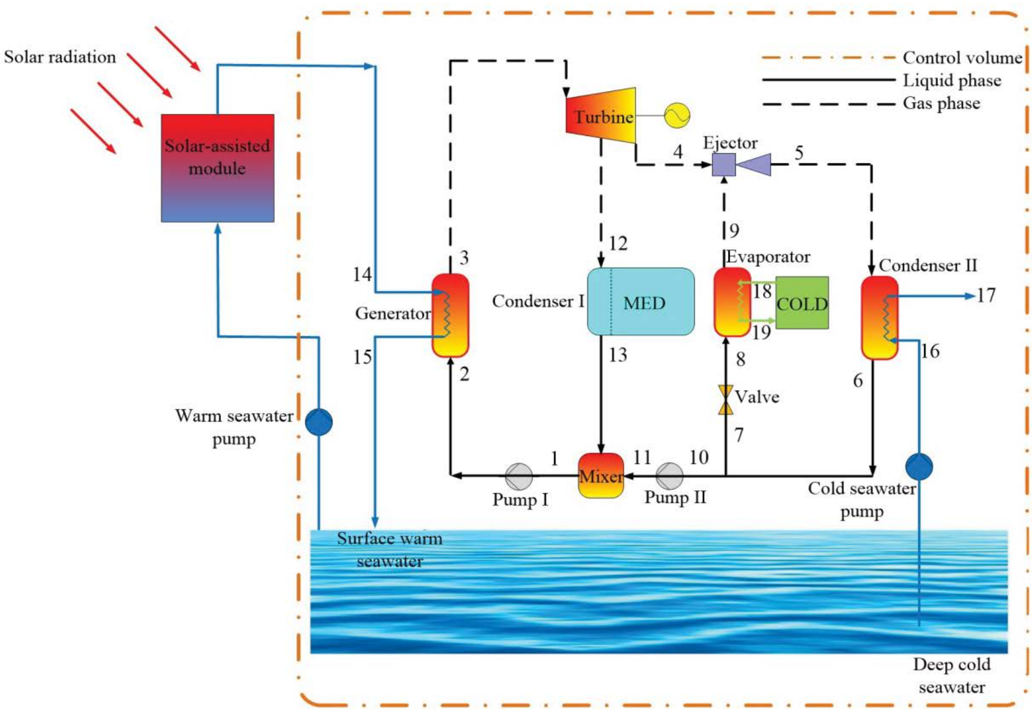

Fig. 1. Schematic diagram of the CCDP cycle.

seawater is first introduced to the end condenser for cooling generated vapor of the last effect and then part of it is rejected as cooling seawater. The rest as the feed seawater is equally sprayed on the surface of heat transfer tube in each effect of evaporator, and then flows from the top row to the bottom. In the meantime, a small amount of vapor is formed from the feed seawater due to the heat supply from condensation of the steam inside the tube. After that, the generated vapor enters the tube pass of next effect for realizing the utilization of latent heat because of the pressure difference between the adjacent effects. Moreover, the brine at the bottom of evaporator or the condensate inside the tube flows into the bottom of next effect or the corresponding flashing box for heat recovery. Then the vapor formed by flashing will be combined with the vapor generated on the surface of heat transfer tube as the heat source of next effect. The process described above is repeated until the final evaporator. At the end, the distillate as product is collected and the cumulative brine is discharged.

3. Mathematical modeling

Detailed thermodynamic and economic model of the proposed CCDP cycle is carried out in this section based on the assumptions and characteristics as follows:

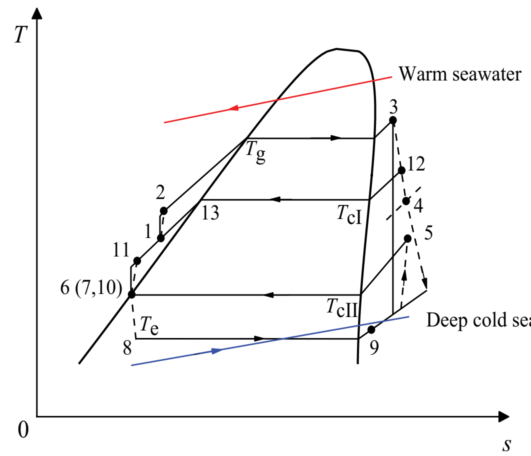

Fig. 2. T-s diagram for the CCDP cycle using dry working fluid.

- The proposed cycle runs under steady-state conditions.
- All liquids are incompressible.
- There are no pressure drop in pipes and heat losses to the environment, but the thermodynamic losses in MED are taken into account, including boiling point elevation and the pressure drops of vapor flowing between adjacent effects [25].
- There is no leakage of working fluid in the combined cycle.
- The power consumption of seawater pumps and MED unit is considered.

3.1. Mass, energy and exergy balances

The balances of mass, salinity and energy of each component in MED unit are given in Table 1 [26], and Table 2 lists the thermodynamic equations for the other components of the CCDP cycle. Wherein, m, x, Q, h, λ, W, η and μ denote mass flow rate, salinity, heat transfer rate, specific enthalpy, latent heat, power, efficiency, and the entrainment ratio, respectively. The subscripts of f, d, bf, df, b, c, cI, w1,

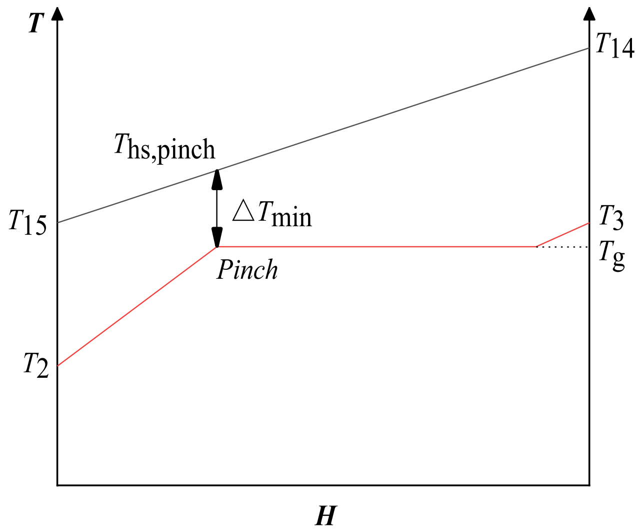

Fig. 4. T-H diagram of generator.

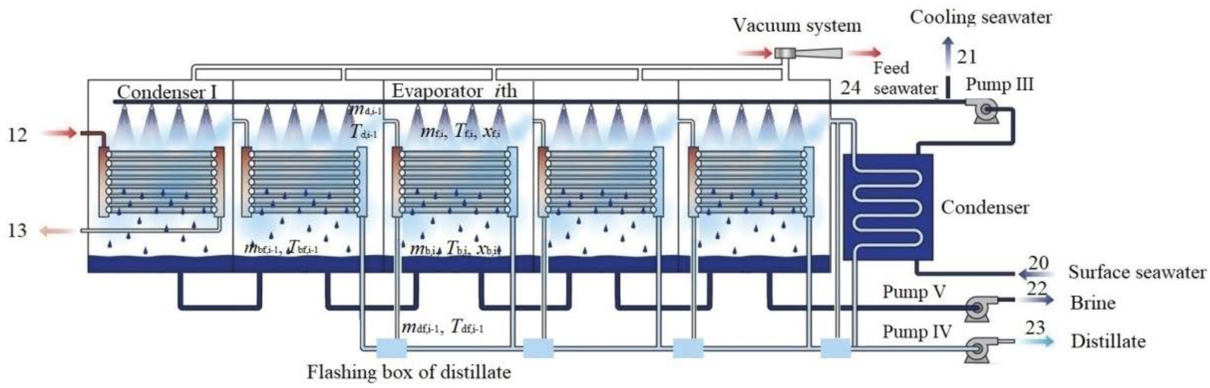

Fig. 3. Schematic diagram of MED.

Table 1
Conservation equations for MED

Component	Mass, salinity and energy balance equations	No.
Condenser I	$m_{f,1} = m_{d,1} + m_{b,1}$	(1)
(the first effect)	$m_{f,1}x_{f,1} = m_{b,1}x_{b,1}$	(2)
	$Q_{cI} = m_{w1} (h_{12} - h_{13}) = m_{f,1} (h_{b,1} - h_{f,1}) + m_{d,1}\lambda_{d,1}$	(3)
The *i*th effect of	$m_{f,i} = m_{d,i} + m_{b,i}$	(4)
evaporator	$m_{f,i}x_{f,i} = m_{b,i}x_{b,i}$	(5)
	$m_{d,i-1}\lambda_{d,i-1} + m_{df,i-1}\lambda_{df,i-1} + m_{bf,i-1}\lambda_{bf,i-1} = m_{f,i} (h_{b,i} - h_{f,i}) + m_{d,i}\lambda_{d,i}$	(6)
	$m_{bf,i}\lambda_{bf,i} = m_{b',i-1} (h_{b,i-1} - h_{bf,i})$, $i = 2,\ldots,n$	(7)
Flashing box of distillate	$m_{df,i}\lambda_{df,i} = m_{d',i-1} (h_{c,i-1} - h_{df,i})$, $i = 2,\ldots,n$	(8)
Condenser	$m_{d,n}\lambda_{d,n} + m_{bf,n}\lambda_{bf,n} + m_{df,n}\lambda_{df,n} = m_{20} (h_{24} - h_{20})$	(9)

Table 2
Mass and energy balance equations applied to the other components of the CCDP cycle

Component	Mass and energy balance equations	No.
Generator	$m_{hs} = m_{14} = m_{15}$, $m_w = m_2 = m_3$	(10)
	$Q_g = m_{hs} (h_{14} - h_{15}) = m_w(h_3 - h_2)$	(11)
Turbine	$W_{tur} = m_w (h_3 - h_{12})\eta_{tur} + (m_w - m_{w1})(h_{12} - h_4)\eta_{tur}$	(12)
	$\eta_{is,tur} = (h_3 - h_{12})/(h_3 - h_{12,is}) = (h_{12} - h_4)/(h_{12} - h_{4,is})$	(13)
Ejector [27]	$m_5 = m_4 + m_9$	(14)
	$(1 + \mu)h_5 = h_4 + \mu h_9$	(15)
	$\mu = m_9 / \left(m_w - m_{w1}\right) = \sqrt{\eta_n\eta_m\eta_d\left(h_{pf,n1} - h_{pf,n2,is}\right) / \left(h_{mf,d,is} - h_{mf,m}\right)} - 1$	(16)
Evaporator	$m_e = m_8 = m_9$, $m_{18} = m_{19}$	(17)
	$Q_c = m_e (h_9 - h_8) = m_{cold} (h_{19} - h_{18})$	(18)
Valve	$m_7 = m_8$, $h_7 = h_8$	(19)
Condenser II	$m_5 = m_6$, $m_{16} = m_{17}$	(20)
	$Q_{cII} = m_5 (h_5 - h_6) = m_{cw} (h_{17} - h_{16})$	(21)
Mixer	$m_1 = m_{11} + m_{13}$	(22)
	$Q_{mix} = m_w h_1 = w_{m1}h_{13} + (m_w - m_{w1})h_{11}$	(23)

b′, *d′*, *g*, hs, cw, *w*, tur, *c*II, *e* and mix stand for feed seawater, generated vapor in the evaporator, vapor flashed off from the brine and the distillate, brine, vapor condensed, condenser I, extraction vapor, accumulated brine and distillate, generator, pre-heated warm seawater, deep cold seawater, working fluid in generator, turbine, condenser II, evaporator and mixer, respectively.

In Table 2, the mass flow rate of working fluid in generator m_w can be obtained by Eqs. (24) and (25) based on the pinch point temperature difference. The T-H diagram of heat transfer process for generator is shown in Fig. 4.

$$m_w = \frac{m_{hs}\left(h_{14} - h_{hs,pinch}\right)}{\left(h_3 - h_{pinch}\right)} \quad (24)$$

$$T_{hs,pinch} = T_g + \Delta T_{min} \quad (25)$$

The turbine outlet pressure p_4 can be obtained by dividing the generation pressure P_g by the expansion ratio β:

$$p_4 = \frac{p_g}{\beta} \quad (26)$$

The extraction ratio R_{et} is defined as the ratio of mass flow rate of the extracted and inlet working fluids of turbine as follows:

$$R_{et} = \frac{m_{w1}}{m_w} \quad (27)$$

The exergy destruction equations of main components of the CCDP cycle are listed in Table 3, where *I* stands for exergy destruction, and the exergy of each state point can be obtained by Eq. (28).

Table 3
Exergy destruction of each component of CCDP system

Component	Exergy destruction equations	No.
Generator	$I_g = T_0\,[m_w\,(s_3 - s_2) + m_{hs}\,(s_{16} - s_{15})]$	(29)
Turbine	$I_{tur} = T_0\,[m_{w1}\,(s_{12} - s_3) + (m_w - m_{w1})(s_4 - s_3)]$	(30)
Ejector	$I_{eje} = T_0\,(m_w - m_{w1})[(1 + \mu)\,s_5 - (s_4 + \mu s_9)]$	(31)
Evaporator	$I_e = T_0\,[m_e\,(s_9 - s_8) + m_{19}\,(s_{19} - s_{18})]$	(32)
Valve	$I_v = T_0\,(m_w - m_{w1})\mu\,(s_8 - s_7)$	(33)
Condenser II	$I_{cII} = (m_w - m_{w1})(1 + \mu)[(h_5 - h_6) - T_0\,(s_5 - s_6)]$	(34)
Mixer	$I_{mix} = T_0\,[m_w s_1 - (m_{w1} s_{13} + (m_w - m_{w1}) s_{11})]$	(35)
Pumps	$I_{pI} = T_0 m_w\,(s_2 - s_1)$	(36)
	$I_{pI} = T_0\,(m_w - m_{w1})(s_{11} - s_{10})$	(37)
MED	$I_{MED} = m_{w1}\,[(h_{12} - h_{13}) - T_0(s_{12} - s_{13})] + E_{20} - E_{X,D} - E_{21} - E_{23}$	(38)

$$E = m\left[\left(h-h_0\right)-T_0\left(s-s_0\right)\right] \tag{28}$$

3.2. Pumping power consumption

In the proposed system, power consumption of the pumps should be noticeable in order to predict the net power output more accurately.

Working fluid pumps:

$$W_{pI} = \frac{m_w\left(h_{2,is}-h_1\right)}{\left(\eta_{is,pump}\eta_{pump}\right)} \tag{39}$$

$$W_{pII} = \frac{\left(m_w - m_{w1}\right)\left(h_{11,is}-h_{10}\right)}{\left(\eta_{is,pump}\eta_{pump}\right)} \tag{40}$$

where $\eta_{is,pump}$ and η_{pump} represent the isentropic efficiency of working fluid pumps and the efficiency of pump motor, respectively.

Seawater pumps [16]:

$$W_{hs(cw)} = \frac{m_{hs(cw)}\Delta P_{hs(cw)}}{\left(\rho_{hs(cw)}\eta_{swp}\eta_{motor,swp}\right)} \tag{41}$$

$$\Delta P_{hs(cw)} = \frac{f_{hs(cw)}\rho_{hs(cw)}L_{hs(cw)}V_{hs(cw)}^{\;2}}{\left(2d_{hs(cw)}\right)} \tag{42}$$

where ΔP stands for the pressure drop of seawater pipelines and f is the friction factor [28]. $\eta_{motor,swp}$ and η_{swp} are the motor efficiency and seawater pumps efficiency. V, d and L stand for flow velocity, diameter and length of the seawater pipeline, respectively. The length of pipeline L can be determined by the relationship between depth and seawater temperature as shown in Fig. 5, where the data are obtained from Wu et al. [29]. According to the piping design specifications, the flow velocity V in the pipeline ranges from 1.0 to 2.0 m/s, and 1.0 m/s is chosen in this work to calculate the $d_{hs(cw)}$ [30]:

$$d_{hs(cw)} = \sqrt{\frac{4m_{hs(cw)}}{\left(\pi\rho_{hs(cw)}V\right)}} \tag{43}$$

where ρ is the density of seawater.

In this work, the power consumption of the pumps in MED unit, including intake seawater pump (Pump III), distillate extraction pump (Pump IV), brine blowdown pump (Pump V) and vacuum pump, is taken into account [31]:

$$W_{MED} = \frac{\Delta P_{pf}\dot{V}_{pf} + \Delta P_{pb}\dot{V}_{pf} + \Delta P_{pd}\dot{V}_{pd} + \left(P_0 - P_{c,N}\right)\dot{V}_{pv}}{\eta_{pump,MED}\,\eta_{motor,MED}} \tag{44}$$

Table 4
Equipment costs of the MED unit

Equipment	Equation	No.
Evaporators [34]	$Z_{evaporators} = 240 \times \sum_{i=1}^{N} A_i$	(45)
Condenser [34]	$Z_{condenser} = 240 \times A$	(46)
Distillate flashing box [35]	$Z_{flash} = \sum_{i=2}^{n} 40{,}745 \times \left(M_{d',i-1}\right)^{0.3}$	(47)
Pumps of MED unit [35]	$Z_{MED,pumps} = 3{,}516 \times (W_{MED})^{0.65}$, $W_{MED} \le 224$ kW $Z_{MED,pumps} = 50{,}000 + 234.5 \times W_{MED}$, $W_{MED} > 224$ kW	(48)

Table 5
Purchasing costs of the other major equipment for the CCDP system

Component	Purchase cost function	No.
Generator [36]	$\log Z_{gen} = 4.6656 - 0.1557\log A + 0.1547 \times (\log A)^2$	(49)
Turbine [37]	$\log Z_{tur} = 2.6259 + 1.4398\log W - 0.1776 \times (\log W)^2$	(50)
Ejector [38]	$Z_{eje} = 16.14 \times 989 m_5 \left(\frac{T_9}{p_9}\right)^{0.05} p_5^{-0.75}$	(51)
Evaporator [37]	$\log Z_{eva} = 130\ (A/0.093)^{0.78}$	(52)
Condenser II [36]	$\log Z_{cII} = 4.6656 - 0.1557\log A + 0.1547 \times (\log A)^2$	(53)
Working fluid pumps [39]	$\log Z_{pump} = 3.8696 + 0.3161\log W + 0.122 \times (\log W)^2$	(54)
Seawater pumps [36]	$\log Z_{seawater\ pump} = 3.3892 + 0.0536\log W + 0.1538 \times (\log W)^2$	(55)

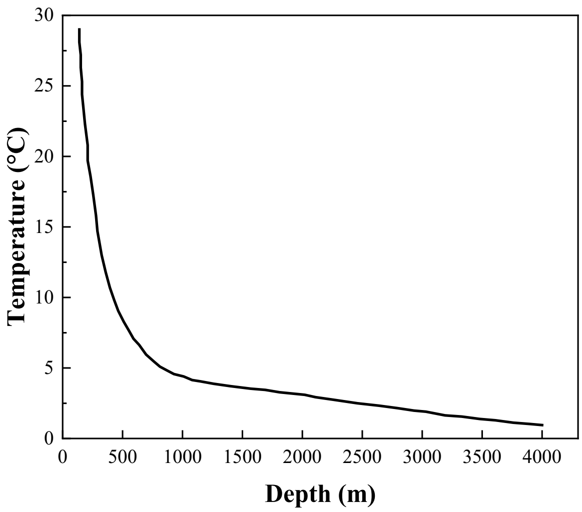

Fig. 5. Relationship between depth and temperature of ocean.

where ΔP and $\dot{V}$ are the pressure difference and volumetric flow rate in pumps, respectively. $\eta_{pump,MED}$ and $\eta_{motor,MED}$ stand for the pump and motor efficiencies. The subscripts of pf, pb, pd and pv denote intake seawater pump, brine blowdown pump, distillate extraction pump and vacuum pump, respectively. The value of ΔP_{pf}, ΔP_{pb} and ΔP_{pd} is generally set as 150, 200 and 200 kPa in MED desalination plant [32]. The mass flowrate of the non-condensable gas in the desalination system is estimated as 1% of the vapor flowrate in the last effect [33].

3.3. Economic model

The cost equations of MED and other components of the proposed CCDP system are listed in Tables 4 and 5, respectively.

In the present work, plate heat exchanger is chosen for the generator, evaporator and condenser II, the heat transfer area A of which is calculated by the following equation:

$$A = \frac{Q}{U\Delta T_{ln}} \tag{56}$$

where U stands for the overall heat transfer coefficient and ΔT_{ln} represents the logarithmic mean temperature difference. In addition, the horizontal-tube falling-film evaporator and shell-and-tube condenser are adopted in MED, the heat transfer coefficients of which are calculated according to our previous work [26].

$\dot{Z}$ is the investment rate, which can be altered from the initial investment Z:

$$\dot{Z} = \text{CRF}\delta Z \tag{57}$$

δ with the value of 1.05 stands for the factor of the operating and maintenance costs [40]. CRF is the capital recovery factor, which is expressed as [41]:

$$\text{CRF} = \frac{j(j+1)^n}{(j+1)^n - 1} \tag{58}$$

where j with the value of 0.062 stands for the discount rate [42]. n refers to plant lifetime of the proposed cycle, which is taken as 20 y [43].

3.4. Performance criteria

The system performances can be evaluated by the exergy efficiency η_{ex} and total cost rate (TCR) from the thermodynamic and economic points of view.

The exergy efficiency for the CCDP cycle can be expressed by:

$$\eta_{ex} = \frac{E_{X,w} + E_{X,ref} + E_{X,D}}{E_{X,in}} \tag{59}$$

where the net power output $E_{X,w}$ can be obtained by the turbine output W_{tur} minus the power consumption of MED unit, working fluid pumps and seawater pumps.

$$E_{X,x} = W_{tur} - W_{pI} - W_{pII} - W_{hs} - W_{cw} - W_{MED} \tag{60}$$

The refrigeration exergy $E_{X,ref}$:

$$E_{X,ref} = m_e\left[(h_8 - h_9) - T_0(s_8 - s_9)\right] \tag{61}$$

The exergy of distillate $E_{X,D}$ [44]:

$$E_{X,D} = D\left[\left(h_{D,\text{out}} - h_0\right) - T_0\left(s_{D,\text{out}} - s_0\right)\right] + E_D^{\text{ch}} \quad (62)$$

where E_D^{ch} is the chemical exergy of fresh water.

The exergy input $E_{X,\text{in}}$:

$$E_{X,\text{in}} = m_{\text{hs}}\left[\left(h_{14} - h_{15}\right) - T_0\left(s_{14} - s_{15}\right)\right] \quad (63)$$

The ambient conditions are: T_0 = 25°C, P_0 = 101.3 kPa and x_0 = 32 g/kg.

The TCR for the CCDP cycle is defined as [45]:

$$\text{TCR} = \sum \dot{Z}_k \quad (64)$$

In addition, to further understand the influence of each decision variable on the three subsystems of ORC, ERC and MED, power efficiency η_{net}, coefficient of performance (COP) and performance ratio (PR) are also selected as performance indicators, respectively.

The power efficiency η_{net} is expressed as:

$$\eta_{\text{net}} = \frac{E_{X,x}}{Q_g} \quad (65)$$

The COP for the refrigeration cycle is defined as follows:

$$\text{COP} = \frac{Q_e}{m_w\left(1 - R_{\text{et}}\right)\left(h_4 - h_{10}\right) + W_{p\text{II}}} \quad (66)$$

The PR of MED can be calculated as follows [46]:

$$\text{PR} = \frac{D}{\left(Q_{c\text{I}} / 2{,}330\right)} \quad (67)$$

3.5. Model validation

Based on the mathematical model, a corresponding simulation program is compiled under the MATLAB platform and the thermodynamic properties of the working fluids are obtained by REFPROP 9.0, and the solving framework of which is shown in Fig. 6. The developed model for ORC-ERC subsystem and the seawater desalination subsystem are validated separately with the data from the study by Dai et al. [47] and Bigham et al. [48], and the simulation results are shown in Tables 6 and 7, respectively. The simulation results obtained by the currently used model show excellent accordance with the data in the references, where the maximum deviation is below 2.2%.

3.6. Optimization model

In the present article, the multi-objective optimization of CCDP cycle aims to maximize the exergy efficiency and minimize the total cost rate simultaneously, which can be described as follows:

$$\begin{cases} \text{Max } \eta_{\text{net}} \\ \text{Min TCR} \end{cases} \quad (68)$$

The design parameters, including generation temperature T_g, condensing temperature $T_{c\text{I}}$ and $T_{c\text{II}}$, and evaporating temperature T_e, are taken as the decision variables, the boundaries of which are listed in Table 8.

Genetic algorithms (GA) are intelligent optimization algorithms based on Darwin's natural selection law, which randomly searches for the optimal solution by simulating the natural evolution process. GA has been promoted and applied in many fields because of the characteristics of strong adaptability and good globalization. According to the number of objective functions, GA can be divided into two types: single-objective optimization and multi-objective

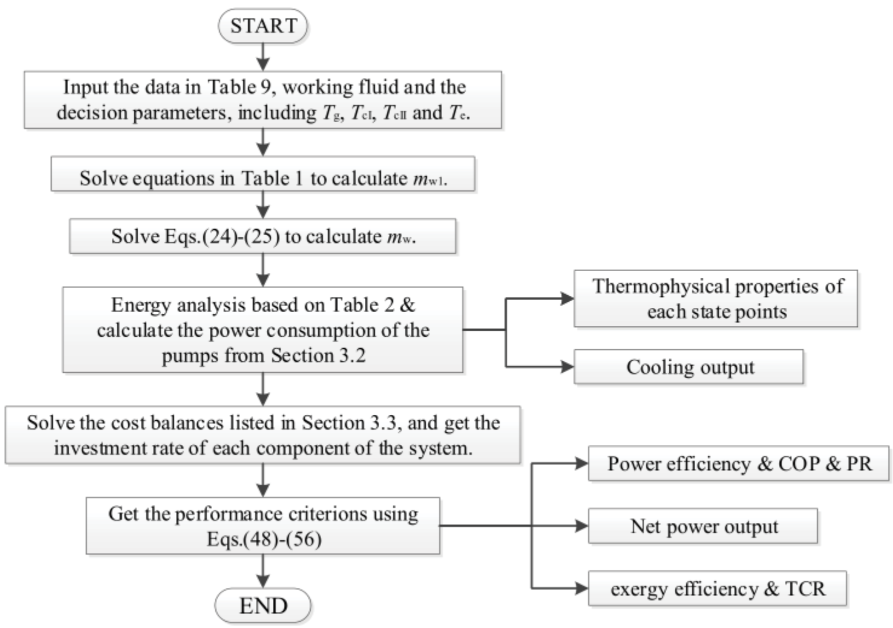

Fig. 6. Solving framework of the CCDP cycle.

Table 6
Comparison between simulation results and data from the study by Dai et al. [47]

State	Temperature (°C)		Pressure (kPa)		Dryness (–)		Mass flow rate (kg/s)	
	Present	Ref.	Present	Ref.	Present	Ref.	Present	Ref.
2	20.45	20.45	800	800	0	0	4.92	4.92
3	140	140	800	800	1	1	4.92	4.92
4	101.65	101.65	200	200	1	1	4.92	4.92
5	92.08	92.08	75.60	75.60	1	1	5.31	5.31
6	20	20	75.60	75.60	0	0	5.31	5.31
7	20	20	75.60	75.60	0	0	0.39	0.39
8	–10	–10	20.20	20.20	0.16	0.16	0.39	0.39
9	–9.90	–10	20.20	20.20	1	1	0.39	0.39
10	20	20	75.60	75.60	0	0	4.92	4.92

Table 7
Comparison between simulation results and data from the study by Bigham et al. [48]

Parameter	Unit	Actual	Present
Number of effects	(–)	4	4
Distillate production	(t/d)	1,536	1,536
Motive steam pressure	(MPa)	1.68	1.68
Salinity of feed seawater	(g/kg)	N/A	32
Concentration ratio	(–)	N/A	1.42
Heat steam temperature	(°C)	65	65
Evaporating temperature in the last effect	(°C)	45.7	45.7
Feed seawater temperature	(°C)	45	45
Surface seawater temperature	(°C)	29	29
Gained output ratio	(–)	6.67	6.80
Specific heat transfer area	(m^2 s/kg)	216	220.6

optimization. For multi-objective optimization, as a result of the trade-off between objective functions, there is often no unique global optimal solution, but an optimal solution set called Pareto frontier set. Non-dominated sorting genetic algorithm with an elite strategy (NSGA-II) has been proved one of the most effective multi-objective optimization algorithms, which can reduce the computational complexity of the algorithm and find better solutions than the other evolution strategies [49].

Based on the established mathematical model, NSGA-II is introduced to solve the multi-objective optimization problem of the proposed CCDP cycle, the algorithm flow chart of which is presented in Fig. 7. Accordingly, a MATLAB program based on NSGA-II is implemented for obtaining the Pareto frontier and the optimal solution set. The number of maximum generations is set as 100, using a search population size of 100 individuals.

4. Results and discussion

In the present study, based on the critical temperature and pressure of working fluid, five working fluids with zero ozone depletion potential are selected and investigated involving dry (R601, R600a and R236ea), wet (R152a) and isentropic (R245fa), which have different slopes of the saturated steam line as shown in Fig. 8. The properties of five working fluids are displayed in Table 9.

In order to investigate the effects of main operating parameters on the thermal performance and introduce the multi-objective optimization, the operation conditions of CCDP are specified as shown in Tables 10 and 11.

4.1. Parametric study

Effects of the generation temperature T_g (with the constant expansion ratio of the turbine) on the performances of CCDP cycle are shown in Fig. 9. It can be seen from Fig. 9a that as the T_g increases, the net power output $E_{X,w}$ gets diminished for the five working fluids and the $E_{X,w}$ for R600a and R152a is higher than the other three. According to the properties of working fluids, the specific enthalpy difference (h_3–h_4) of expansion process in turbine for R152a decreases by 6.99% and that for the others almost remain the same (no more than 2%) with T_g varying from 90°C to 102°C, based on a constant expansion ratio. Meanwhile,

Table 8
Decision variables and their boundaries

Decision variables	Unit	Lower bound	Upper bound	Base case
Generation temperature, T_g	(°C)	90	102	100
Condensing temperature of condenser I, T_{cI}	(°C)	62	75	70
Evaporating temperature, T_e	(°C)	–10	10	10
Condensing temperature of condenser II, T_{cII}	(°C)	20	36	30

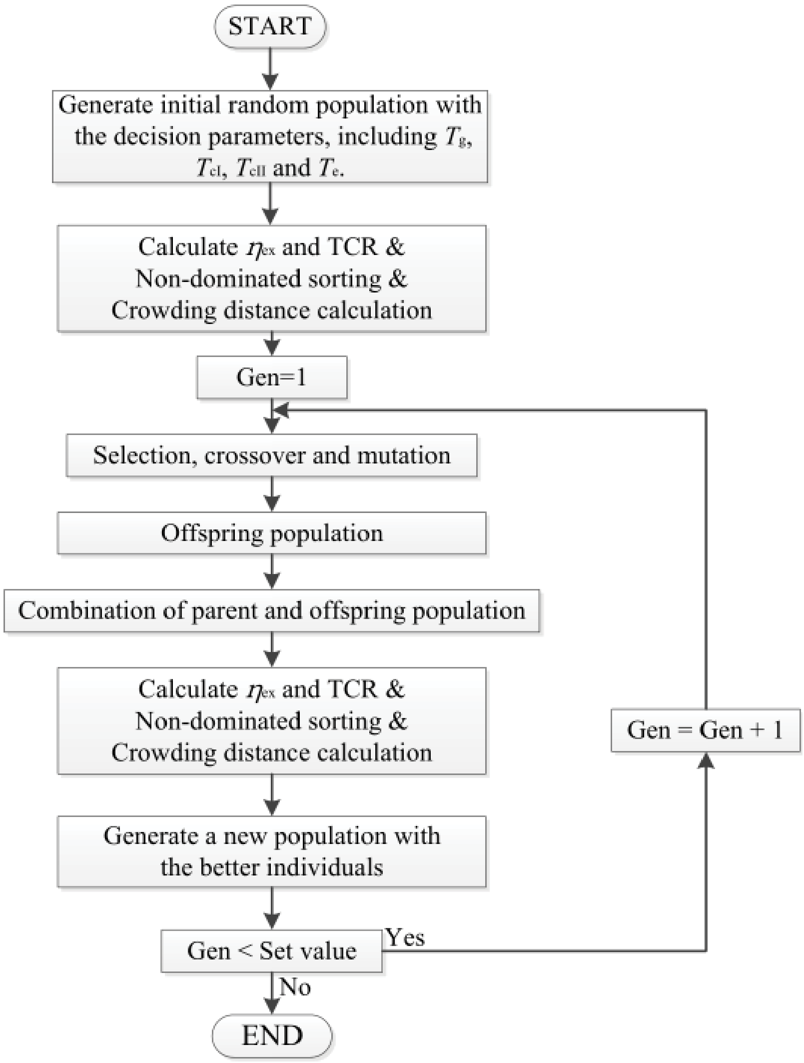

Fig. 7. Algorithm flow chart of NSGA-II.

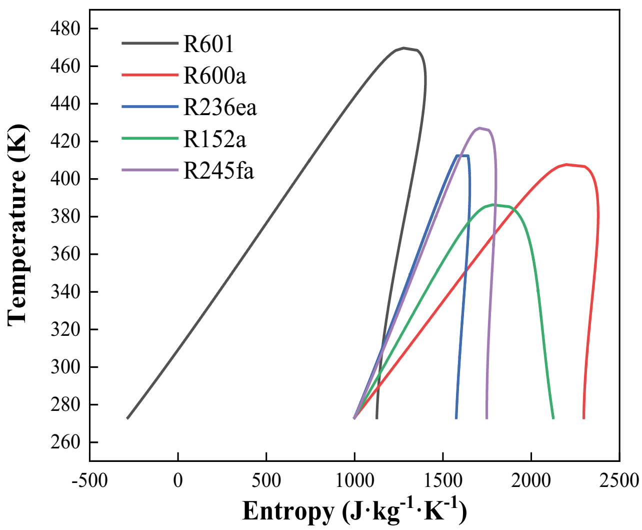

Fig. 8. T-s plots of different working fluids.

according to Eqs. (24) and (25), the rise of T_g leads to the decreasing mass flow rate m_w of working fluid in generator. As a result, the $E_{X,w}$ decreases. At the same T_g, the latent heat of evaporation of R601 is the highest, followed by R600a, R152a, R245fa and R236ea. Correspondingly, the mass flow rate m_w presents an opposite order. Furthermore, the largest specific enthalpy difference (h_3–h_4) belongs to R600a, followed by R601, R152a, R245fa and R236ea. Because m_w and (h_3–h_4) vary at different paces, the $E_{X,w}$ for the five working fluids show the tendency as described above. On the premise of constant pinch temperature difference of generator, the increase of T_g leads to a higher outlet temperature of warm seawater, and thus the heat transfer capacity Q_g in generator decreases according to Eq. (11) (Fig. 9d). Differing from the trends for the other working fluids, the power efficiency η_{net} for R600a and R152a descends because the decreasing rate in $E_{X,w}$ is greater than that of Q_g.

As shown in Figs. 9b and c, the cooling capacity Q_e and refrigeration exergy $E_{X,ref}$ of R601, R245fa and R236ea decrease with the increase of T_g, and the Q_e and $E_{X,ref}$ of R600a and R245fa increase first and then decrease. The maximum Q_e is

Table 9
Properties of working fluids for the CCDP cycle

Working fluids	Chemical formula	Critical temperature (°C)	Critical pressure (MPa)	Remark
R601	C_5H_{12}-1	196.50	3.36	Dry
R600a	C_4H_{10}-2	134.65	3.63	Dry
R236ea	$C_3H_2F_6$	139.23	3.41	Dry
R152a	$C_2H_4F_2$	113.30	4.52	Wet
R245fa	$C_3H_3F_5$-D1	154.00	3.65	Isentropic

Table 10
Specifications of CCDP cycle

Parameter	Unit	Value
Mass flow rate of warm seawater, m_{14}	(kg/s)	65
Inlet temperature of the warm seawater, T_{14}	(°C)	120
Inlet temperature of the deep cold seawater, T_{16}	(°C)	4.5
Outlet temperature of the deep cold seawater, T_{17}	(°C)	13
Degree of supercooling in the condenser II, ΔT_{con}	(°C)	1
Minimum temperature difference in generator, ΔT_{min}	(°C)	5
Degree of superheat in the generator, ΔT_{gen}	(°C)	3
Expansion ratio of the turbine, β	(–)	2.6
Degree of superheat in the evaporator, ΔT_{eva}	(°C)	1
Length of warm seawater pipeline, L_{hw}	(m)	100
Length of deep cold seawater pipeline, L_{cw}	(m)	1,000
Salinity of dead state, x_0	(g/kg)	32
Environment pressure, P_0	(MPa)	0.1
Environment temperature, T_0	(°C)	
Overall heat transfer coefficient for the evaporator, U_{eva}	(kW/m^2 K)	4
Overall heat transfer coefficient for the generator, U_{gen}	(kW/m^2 K)	4
Overall heat transfer coefficient for the condenser II, U_{con}	(kW/m^2 K)	2
Nozzle, mixing and diffuser efficiency of ejector, η_n, η_m, η_d	(%)	95, 90, 88
Mechanical and isentropic efficiency of turbine, η_{tur}, $\eta_{tur,is}$	(%)	96, 85
Isentropic and efficiency of working fluid pumps, $\eta_{pump,is}$, η_{pump}	(%)	80, 78
Pump and motor efficiency of seawater pumps, η_{swp}, $\eta_{motor,swp}$	(%)	85, 95
Pump and motor efficiency for MED $\eta_{pump,MED}$, $\eta_{motor,MED}$	(%)	70, 90

Table 11
Specifications of MED

Parameter	Unit	Value
Salinity of feed seawater, x_f	(g/kg)	32
Evaporating temperature in the last effect, $T_{d,N}$	(°C)	40
Concentration ratio	(–)	1.5
Number of effects, N	(–)	5
Surface seawater temperature, T_{20}	(°C)	25
Distillate production, D	(t/d)	500

about 605.25 and 776.85 kW obtained at T_g of 92°C for R600a and R245fa, respectively. Since the expansion ratio of turbine is set constant, the temperature T_4 of turbine outlet, namely the temperature of motive steam for ejector, climbs with the rising T_g, resulting in an increase in entrainment ratio μ of ejector. This is why the Q_e and $E_{X,ref}$ of R600a and R245fa increase at first. In the meantime, the extraction ratio R_{et} of turbine increases with the decreasing mass flow rate m_w of working fluid, due to the constant distillate production D. Therefore, the mass flow rate (m_w–m_{w1}) of turbine outlet reduces, the decreasing rate of which is higher than the increasing rate of μ. As a result, both Q_e and $E_{X,ref}$ go down at higher T_g because of less working fluid used to refrigerate. Moreover, COP also increases with T_g due to the increasing entrainment ratio.

Regarding to Fig. 9c, with the increase of T_g, the exergy efficiency η_{ex} is decreased for all the working fluids. The highest η_{ex} belongs to R600a, which reaches 27.41% when T_g is 90°C, and as T_g goes up from 90°C to 102°C, it drops by 12.22%. The reason is that the decrement of $E_{X,w}$ and $E_{X,ref}$ is greater than that of total exergy input. For R600a and R152a, η_{ex} decreases sharply than the other

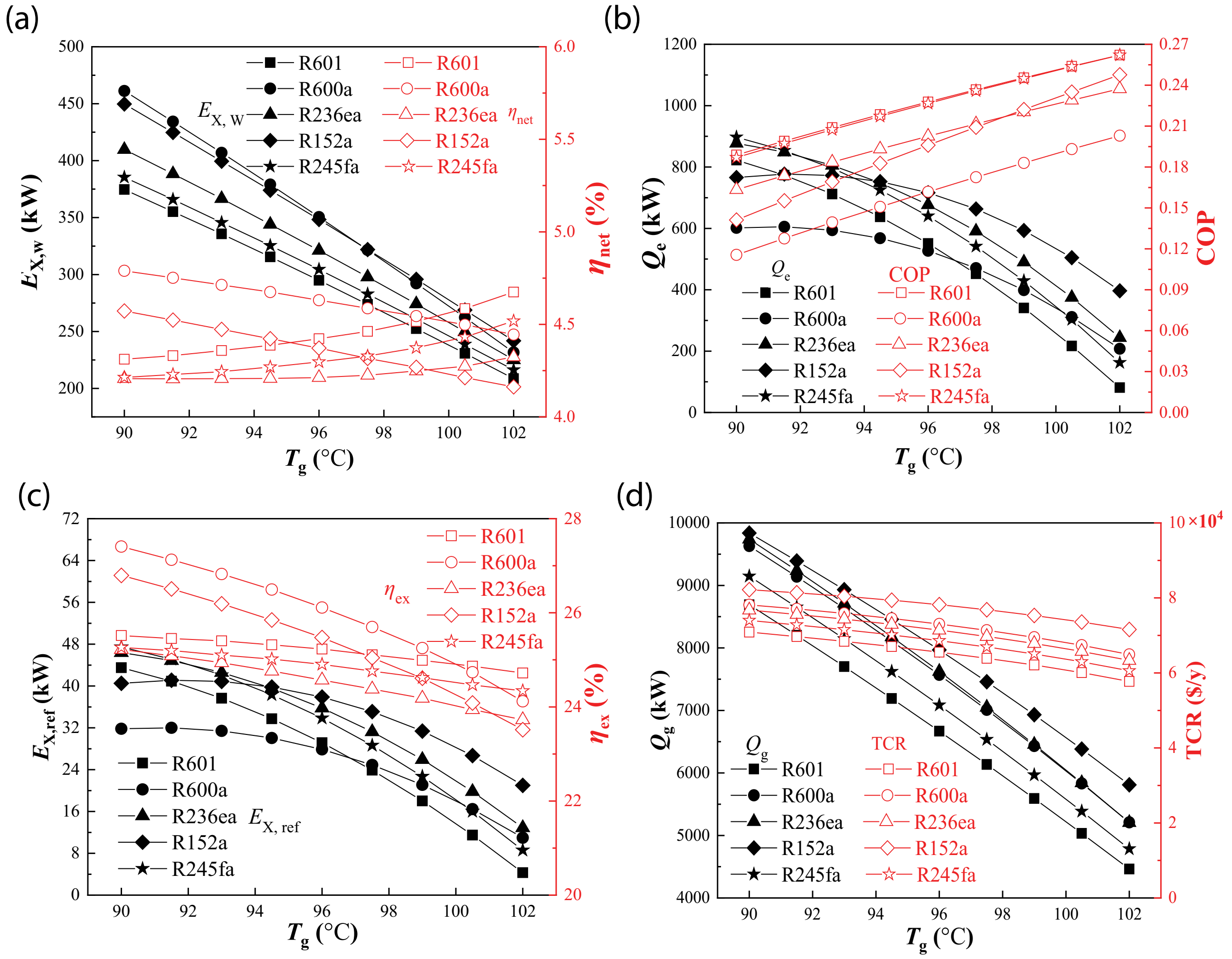

Fig. 9. Effects of the generation temperature on the performances of CCDP cycle: (a) $E_{X,w}$ and η_{net}, (b) Q_e and COP, (c) $E_{X,ref}$ and η_{ex}, and (d) Q_g and TCR.

working fluids, which is mainly caused by the more significant decreasing rates of $E_{X,w}$ (Fig. 9a).

As described in Fig. 9d, it can be found that TCR decrease with T_g for all the five working fluids, and the TCR for R601 is the lowest. As T_g rises from 90°C to 102°C, TCR drops by 18.53%. With T_g increasing, the reduction of heat loads of generator, evaporator and condenser cuts down the required heat transfer areas, and less amounts of working fluids passing though the turbine and ejector bring about smaller device sizes. Therefore, the TCR goes down because of the decline of initial capital costs.

Effects of the condensing temperature of condenser I T_{cI}, namely the temperature of heating steam for the first effect of MED, on the performances of CCDP cycle are illustrated in Fig. 10. As seen in Fig. 10a, PR of MED decreases with the increase of T_{cI}. For MED unit, since the evaporation temperature of last effect (the 5th effect) keeps constant, all the evaporation temperatures of 1st to 4th effects increase with the increase of T_{cI}, which leads to more heat consumption for preheating the feed seawater to the saturation temperature. Meanwhile, according to the physical properties of saturated steam, with the increase of T_{cI}, the latent heat of saturated steam decreases. As a result, both the mass flow rate of extracted vapor m_{w1} and the extraction ratio R_{et} increase. The m_{w1} for five working fluids are inversely related to the latent heat.

As shown in Figs. 10b and c, it can be found that higher T_{cI} leads to smaller net power output and lower cooling capacity, and R152a always has the highest $E_{X,w}$ and Q_e among the five working fluids. As T_{cI} increases from 62°C to 75°C, $E_{X,w}$ and Q_e of R152a decrease by 36.37% and 30.65%, respectively. The reason for the decline of $E_{X,w}$ is the enhancement in R_{et} and the decrease in the specific enthalpy difference (h_3–h_{12}) between turbine inlet and extraction for MED. Additionally, the decreasing mass flow rate of working fluid entering the ejector leads to the reduction in Q_e.

Raising T_{cI} can also lead to an increase in the specific enthalpy h_2 of generator inlet, so energy consumption of the proposed cycle Q_g has a decrease (Fig. 10e). However, the effect of decreasing $E_{X,w}$ is more dominated than that of Q_g, which results in the decline in power efficiency. At the same time, there is an imperceptible effect of T_{cI} on COP, owing to the constant entrainment ratio.

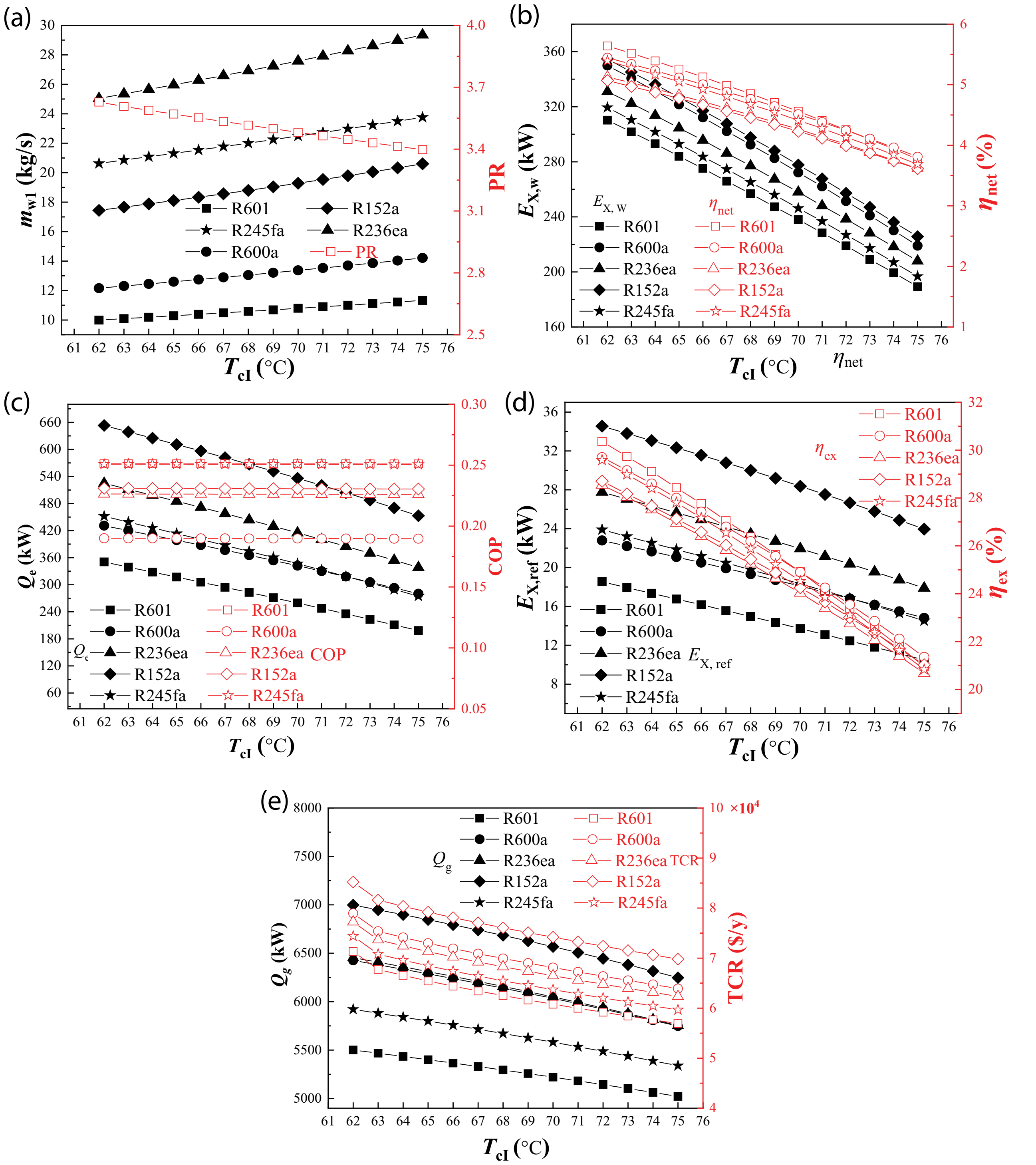

Fig. 10. Effects of the condensing temperature of condenser I on the performances of CCDP cycle: (a) m_{w1} and PR, (b) $E_{X,w}$ and η_{net}, (c) Q_e and COP, (d) $E_{X,ref}$ and η_{ex}, and (e) Q_g and TCR.

Fig. 10d indicates that the exergy efficiency η_{ex} for the five working fluids have similar variations. The η_{ex} decreases with the rising T_{cI}, which is mainly caused by the higher exergy destruction of MED as a result of larger temperature difference in each effect. When T_{cI} varies from 62°C to 75°C, the exergy efficiency of R601 decreases by 30.99%.

Fig. 10e demonstrates the variation of TCR with T_{cI}. It can be seen that the increase in T_{cI} contributes to the reduction of TCR. It is mostly attributed to the great decline in capital cost of MED $\dot{Z}_{MED}$. The rise of T_{cI} boosts the growth of temperature difference for heat transfer in each effect, and thus the required heat transfer area of MED falls. Moreover, the capital costs of other components also decrease with T_{cI} as a result of the decreasing heat loads.

Fig. 11 shows the variations of performances of CCDP cycle with the evaporating temperature T_e. It can be found that effects of T_e on Q_e, $E_{X,\mathrm{ref}}$ and COP of the refrigeration subsystem are significant, while $E_{X,w}$, η_{net}, Q_g, η_{ex} and TCR are not quite sensitive to T_e. The increase of T_e augments the entrainment ratio μ of ejector, which leads to the rise of mass flow rate of working fluid and the decline of enthalpy difference between the inlet and outlet of condenser II. Consequently, the power consumption by the cold seawater pumps W_{cw} slightly goes up due to a higher cooling load of condenser. Therefore, the net power output $E_{X,w}$ mildly decreases. What's more, as a result of the increasing μ, both Q_e and COP get raised (Fig. 9b). R152a always has a higher Q_e than the other four working fluids.

Furthermore, as illustrated in Fig. 11c, there is an imperceptible interaction of T_e on exergy efficiency under the combined effect of increasing $E_{X,\mathrm{ref}}$ and decreasing $E_{X,w}$. The highest η_{ex} is still obtained by R601, followed by R600a, R245fa, R152a, and R236ea.

As shown in Fig. 11d, TCR for the five working fluids gets raised with the rising T_e, and the trend is more obvious at higher T_e. With T_e increasing, larger heat transfer area is needed due to the increasing heat loads in condenser II and evaporator and the decreasing temperature difference in evaporator, which results in the variation of TCR.

Effects of the condensing temperature of condenser II T_{cII} on the performances of CCDP cycle are demonstrated in Fig. 12. It can be seen that the increase of T_{cII} promotes the growth of net power output $E_{X,w}$, but leads to the decrease of cooling capacity Q_e. Among all the five working fluids, R152a always has the highest $E_{X,w}$ and Q_e. When T_{cII} increases from 20°C to 36°C for R152a, $E_{X,w}$ has a rise of 2.17%, while Q_e descends by 86.63%. The increase in $E_{X,w}$ is attributed to the reduction of pump work for the deep cold seawater and working fluid which is caused by the decrease of both the entrainment ratio and the specific enthalpy difference in condenser II. Moreover, the mass flow rate of working fluid in evaporator descends due to the decrease of μ, which results in a drop in both Q_e and COP as presented in Fig. 12b. As T_{cII} increases, the

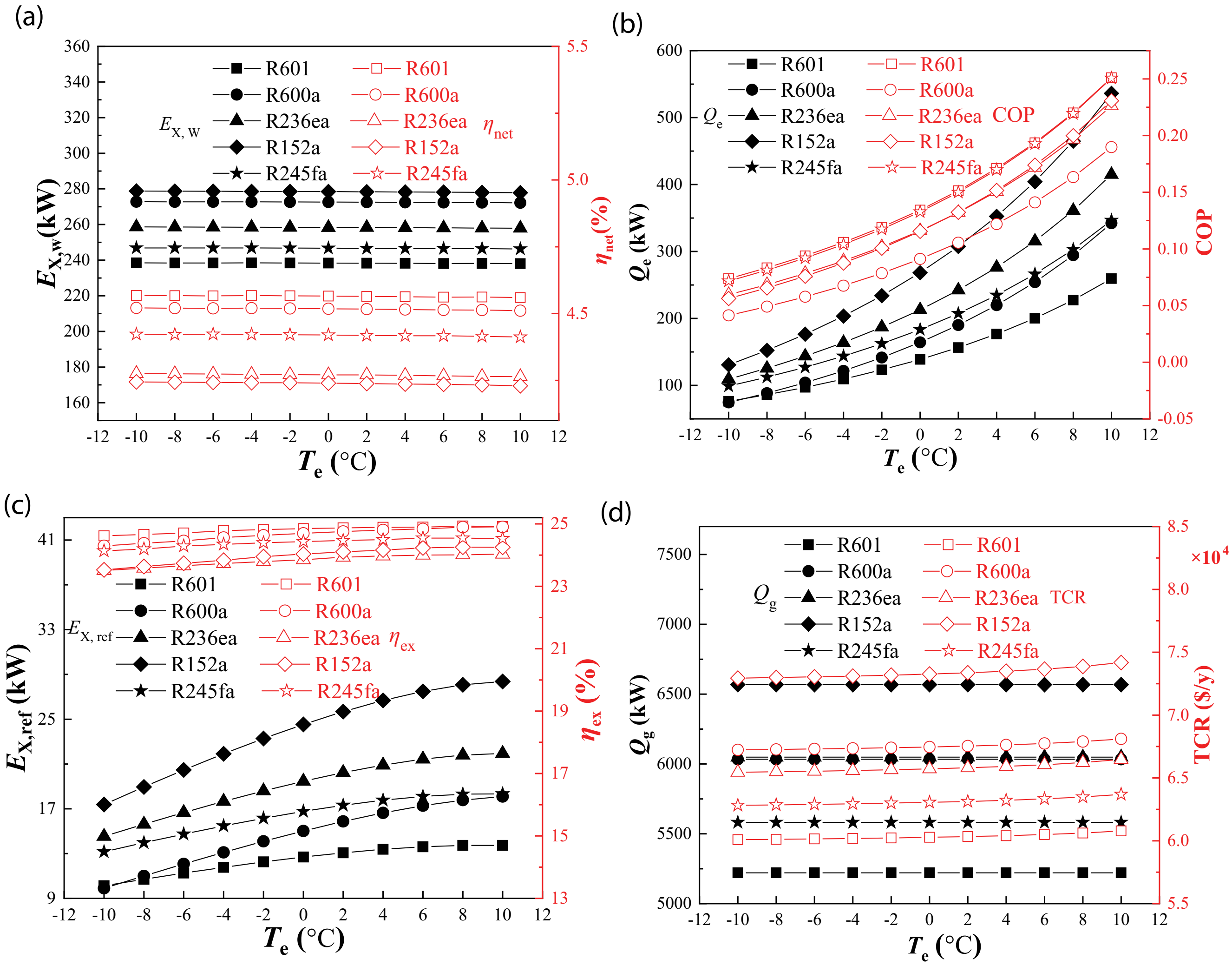

Fig. 11. Effects of the evaporating temperature on the performances of CCDP cycle: (a) $E_{X,w}$ and η_{net}, (b) Q_e and COP, (c) $E_{X,\mathrm{ref}}$ and η_{ex}, and (d) Q_g and TCR.

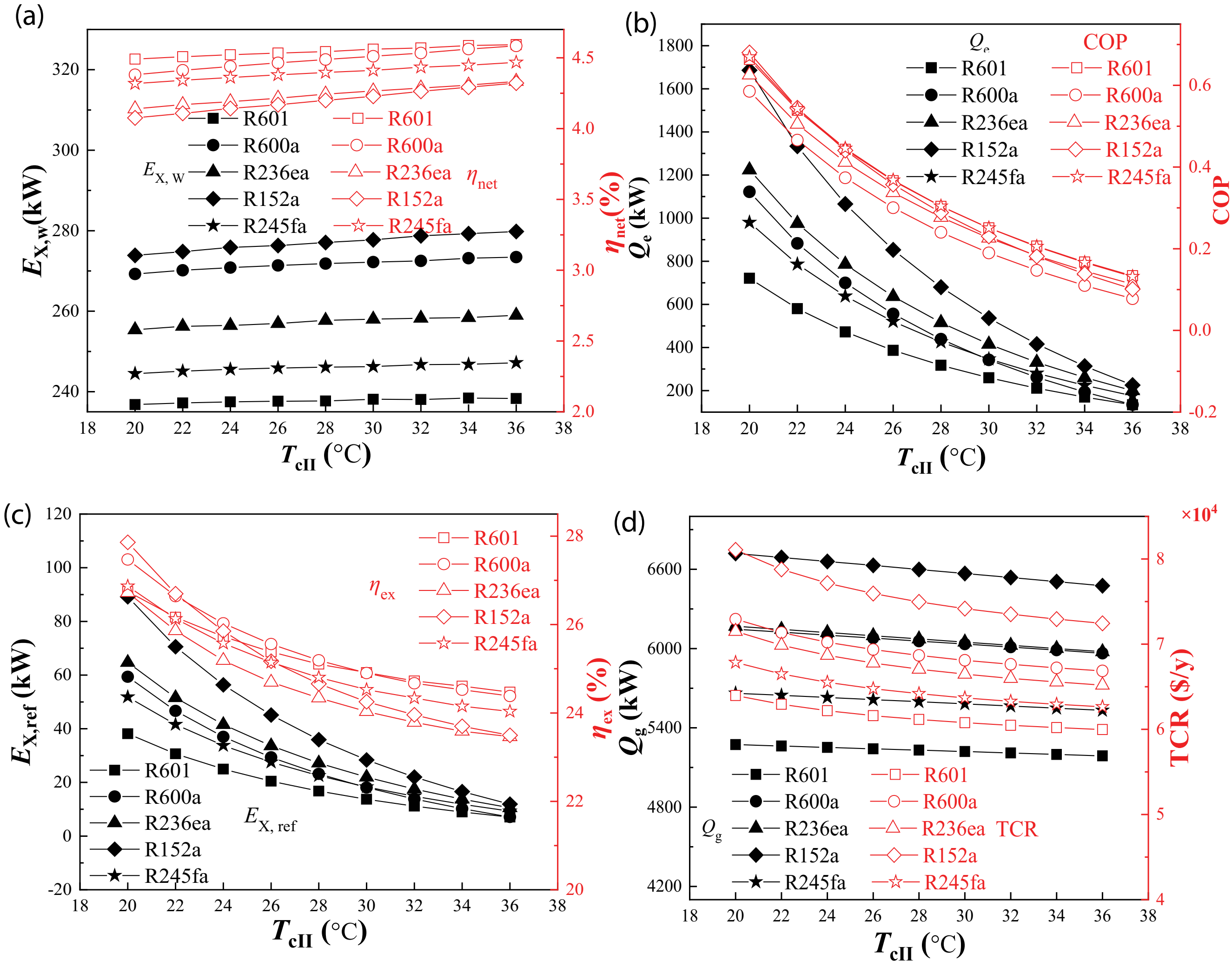

Fig. 12. Effects of the condensing temperature of condenser II on the performances of CCDP cycle: (a) $E_{X,w}$ and η_{net}, (b) Q_e and COP, (c) $E_{X,ref}$ and η_{ex}, and (d) Q_g and TCR.

enthalpy of generator inlet (point 2) rises, which leads to a slight decrease in Q_g (Fig. 12c). Therefore, η_{net} goes up because of the increase of $E_{X,w}$ and the reduction of Q_g.

As can be observed in Figs. 12c and d, both η_{ex} and TCR show declining tendencies with the increasing T_{cII}. Taking R601 as an example, when T_{cII} increases from 20°C to 36°C, TCR and η_{ex} decrease by 6.25% and 8.51%, respectively. The main reason for the drop of η_{ex} is that the exergy destruction of condenser II gets raised by larger temperature difference of heat transfer. Meanwhile, the heat transfer area of condenser II is reduced. In addition, the heat transfer area of evaporator diminishes due to the decreasing of Q_e. As a result, a lower TCR is obtained by the rising T_{cII}.

4.2. Multi-objective optimization

The Pareto frontier set for the CCDP system with five different working fluids is depicted in Fig. 13, which clearly reveals the conflict between exergy efficiency η_{ex} and TCR. Unlike single-objective optimization, the result of multi-objective optimization is a solution set (that is, the Pareto frontier set), and each point on the Pareto frontier curve stands for the potential solution in the search space. Therefore, it is necessary to ascertain the best desired solution point, named POS. Generally, there are three most accepted and ordinary methods to determine the POS, including Shannon's entropy technique, linear programming technique for multi-dimensional analysis of preference (LINMAP) and technique for order preference by similarity to ideal situation [50]. In the present article, LINMAP method is selected for decision-making, which introduces the final desired optimal solution by comparing the geometric distances between each solution in Pareto frontier set and the unreachable ideal solution (Eq. (69)), and the point with the shortest distance u is defined as POS marked in Fig. 13. What's more, the sensitivity of Pareto frontier set regarding to different distillate production loads D is demonstrated in Fig. 13. It can be seen that the tendencies of Pareto frontier set for various D are almost the same: on the left side of POS, with the η_{ex} increasing, the TCR rises slowly; on the right side of POS, further improving the η_{ex} leads to a sharp increase of TCR. Meanwhile,

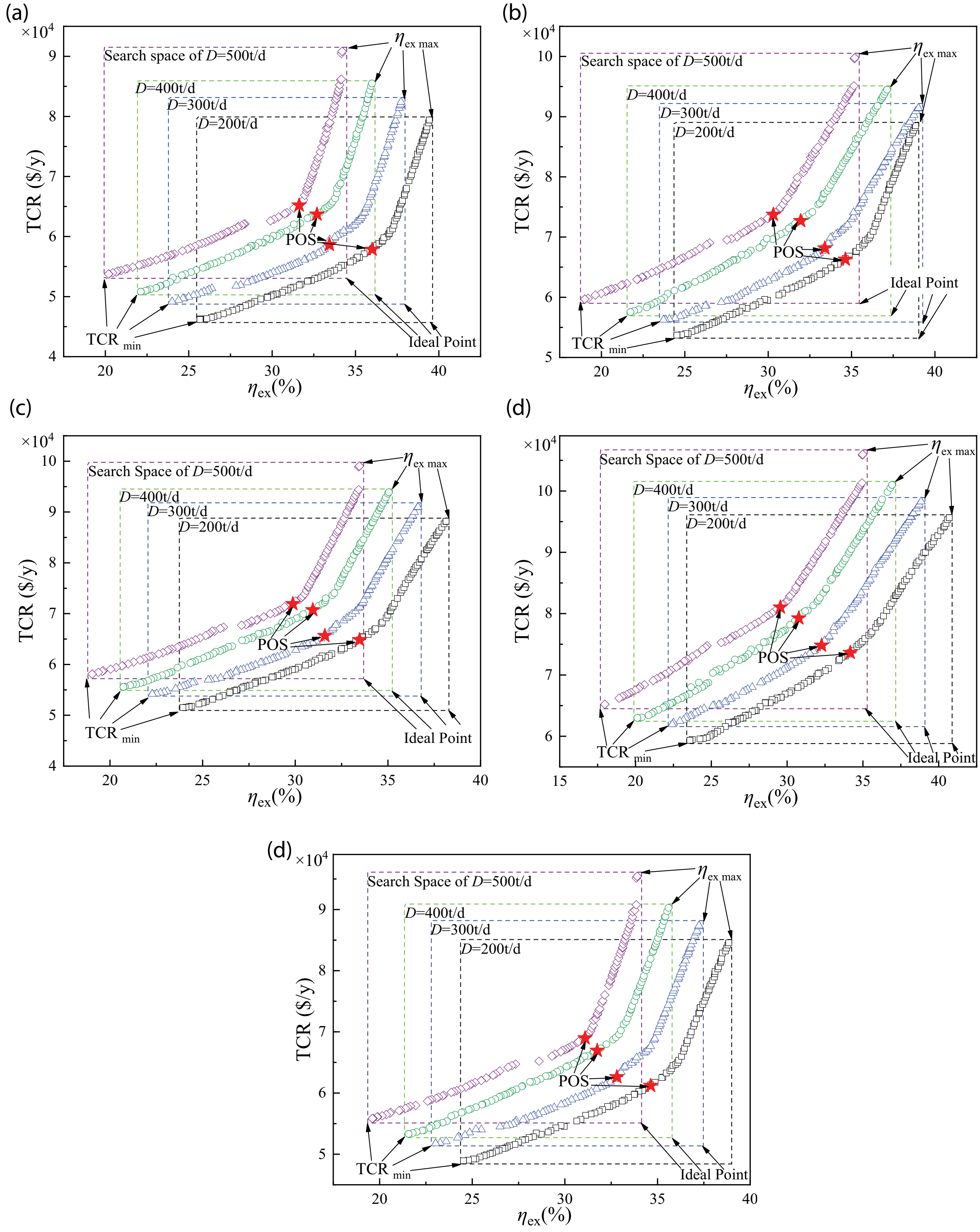

Fig. 13. Pareto frontier for the CCDP cycle with different working fluids: (a) R601, (b) R600a, (c) R236ea, (d) R152a, and (e) R245fa.

larger distillate production load needs higher TCR for the same exergy efficiency.

$$\mathrm{ED}_{u+} = \sqrt{\sum_{v=1}^{n}\left(f_{uv} - f_v^{\mathrm{ideal}}\right)^2} \tag{69}$$

$$u_{\mathrm{POS}} = \arg\min\left(\mathrm{ED}_{i+}\right) \tag{70}$$

where f_v^{ideal} stands for the ideal solution of vth objective in a single-objective optimization, and u represents the number of each solution in Pareto frontier set.

The optimization results of POS, maximum η_{ex} and minimum TCR for five working fluids with D = 500 t/d are listed in Table 12. As observed in the table, both the net power and cooling output of the single-objective optimization for maximizing η_{ex} are higher than that for minimizing TCR, while the POS of multi-objective optimization are situated between them. According to the objective function values of POS, the tested working fluids in this paper are ranked. R601 has the highest exergy efficiency (31.62%) and the lowest TCR (6.51 × 10^4 \$/y), and thus it is first recommended. In addition, R245fa takes the second place with higher η_{ex} (31.09%) and lower TCR (6.89 × 10^4 \$/y) than the other three working fluids, followed by R600a and R236ea. Among all the tested working fluids, the value of POS for R152a is the worst in terms of both TCR and η_{ex}, although it shows good performance on net power and cooling output.

For the Pareto optimal solution of CCDP cycle with R601, the percentage of initial investment for main components and the exergy flows are obtained as shown in Figs. 14 and 15, respectively. It can be seen from Fig. 14 that MED unit is the most expensive with 51.55% of the TCR. Followed by turbine, generator, condenser and pumps, each account for 20.09%, 13.60%, 9.33% and 4.69%, respectively. As displayed in Fig. 15, the exergy flows are divided into three main directions: useful exergy output, exergy destruction and loss. The largest exergy destruction occurs in the MED, which makes up 26.24% of the total exergy input. The exergy destruction in the generator takes the second place due to the insufficient matching of energy grades between the preheated warm seawater and the working fluid. The exergy destruction in ejector is 7.98% as a result of the friction losses and the non-ideal adiabatic expansion. The exergy loss is mainly caused by the discharged non-products and the power consumption of pumps. Almost 7% of total exergy input is lost by rejecting the cooling seawater, brine and cold seawater. Additionally, the exergy loss by pump work is more than 6% of the total exergy input, which makes the net power output significantly lower than the turbine output.

The application background of the proposed CCDP system is providing power, cooling and fresh water for remote islands at low latitudes where both ocean thermal energy and solar energy are abundant. Based on the detailed mathematical models in the present work, the thermodynamic and economic performances of the CCDP system with various distillate productions could be predicted. The multi-objective optimization results can also provide references for making more reasonable design solutions and selection of working fluids.

5. Conclusion

In the present article, a combined cooling, desalination and power system driven by ocean thermal energy has been proposed. Based on the developed mathematical model, a comprehensive study has been carried out from thermodynamic and economic viewpoints. The effects of five different working fluids on the system performance of CCDP cycle under different operating parameters are investigated. Finally, multi-objective optimization for the

Table 12
Optimization results for five working fluids with D = 500t/d

Working fluid	Condition	Design variables				Pareto optimization		$E_{X,w}$ (kW)	E_e (kW)
		T_g (°C)	T_{cI} (°C)	T_e (°C)	T_{cII} (°C)	η_{ex} (°C)	TCR (×10^4 \$/y)		
R601	$\eta_{ex\ max}$	90	62	10	20	34.19	9.08	445.84	153.21
	TCR_{min}	102	75	–7.77	21.63	20.19	5.37	159.94	1.59
	POS	102	62.04	4.52	20.32	31.62	6.51	276.90	21.65
R600a	$\eta_{ex\ max}$	90	62	10	20	35.19	9.97	526.09	155.46
	TCR_{min}	102	75	–10	36	19.00	5.96	173.58	0.47
	POS	102	62.04	3.96	20.51	30.31	7.37	297.04	41.28
R236ea	$\eta_{ex\ max}$	90	62	10	20	33.46	9.90	475.49	179.58
	TCR_{min}	102	75	–10	36	19.04	5.81	171.92	2.07
	POS	102	62.03	1.55	20.04	29.87	7.19	289.16	45.53
R152a	$\eta_{ex\ max}$	90	62	10	20.	34.98	10.59	505.05	184.63
	TCR_{min}	102	75	–7.20	36	17.98	6.52	178.80	3.09
	POS	102	62.36	2.80	20.06	29.55	8.10	295.33	71.02
R245fa	$\eta_{ex\ max}$	90	62	10	20	33.90	9.54	453.55	171.35
	TCR_{min}	102	75	–10	36	19.61	5.88	165.00	1.41
	POS	102	62.04	4.60	20	31.09	6.89	282.48	35.26

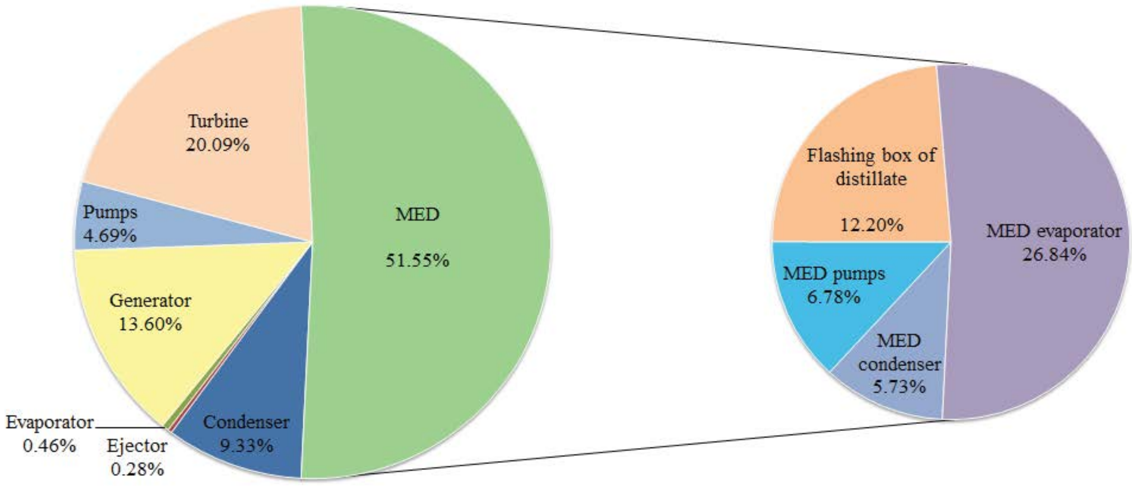

Fig. 14. Percentage of initial investment for main components of CCDP system.

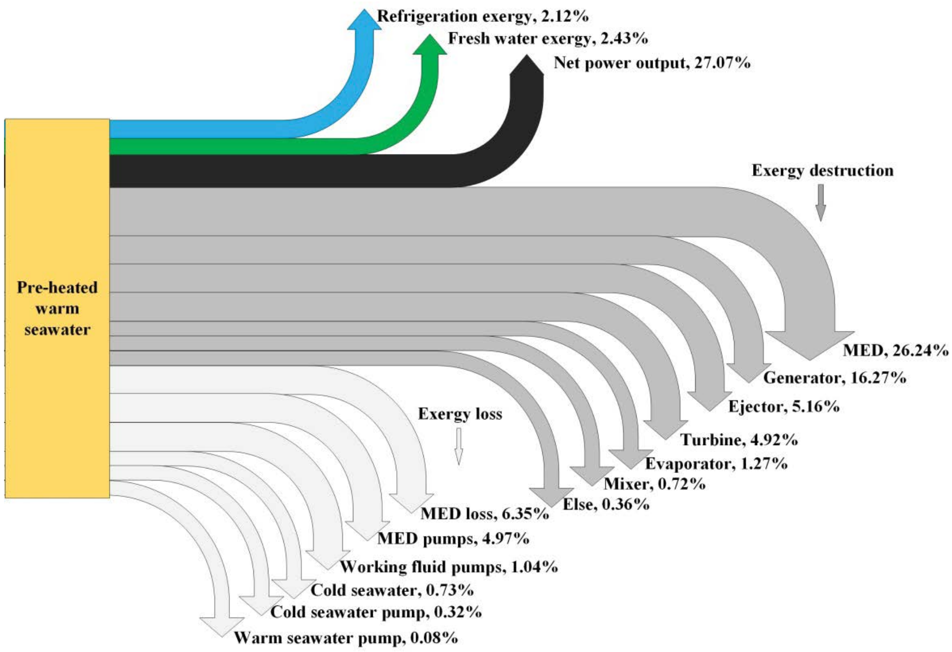

Fig. 15. Exergy flows of CCDP system.

CCDP cycle with various working fluids and distillate productions has been conducted based on NSGA-II algorithm. The exergy efficiency η_{ex} and TCR are taken as objective functions, and the decision variables include generation temperature, condensing temperatures of condenser I and condenser II and evaporating temperature. The main conclusions are summarized as follows:

- The increase of generation temperature T_g has a positive influence on TCR, but leads to a decrease of η_{ex} with constant expansion ratio. The rise of condensing temperatures of condenser I and condenser II results in the decrease of both η_{ex} and TCR. The rising evaporating temperature T_e has little effect on η_{ex}, while it brings about a slight increase of TCR.
- Among the five tested working fluids, R152a is superior to the others in terms of net power and cooling output. R601 always has the lowest TCR, and the highest one belongs to R152a. However, the working fluid corresponding to the highest η_{ex} varies with operating temperature.
- The largest exergy destruction of 26.24% occurs in the MED, followed by the generator and ejector accounting for 16.27% and 5.16%, respectively. The exergy loss by pump work is more than 6% of the total exergy input.
- The POS of the CCDP system has been determined from the Pareto frontier set using LINMAP method. According to the results of POS (with the distillate production of 500t/d), the ranking of five tested working fluids based on exergy efficiency and TCR is as follows:

R601 (31.62% and 6.51 × 10^4 \$/y) has the best performance, followed by R245fa (31.09% and 6.89 × 10^4 \$/y), R600a (30.31% and 7.37 × 10^4 \$/y), R236ea (29.87% and 7.19 × 10^4 \$/y) and R152a (29.55% and 8.10 × 10^4 \$/y).

Symbols

A	—	Heat transfer area, m^2
D	—	Distillate product, t/d
d	—	Diameter of pipeline, m
E	—	Exergy, kW
f	—	Friction factor
h	—	Specific enthalpy, kJ/kg
I	—	Exergy destruction, kW
j	—	Discount rate
L	—	Length of pipeline, m
m	—	Mass slow rate, kg/s
n	—	Plant lifetime, y
P	—	Pressure, kPa
Q	—	Heat load, kW
R	—	Extraction ratio
s	—	Specific entropy, kJ kg^{-1} K^{-1}
T	—	Temperature, °C
U	—	Overall heat transfer coefficient, kW/m^2 K
V	—	Flow velocity, m/s
$\dot{V}$	—	Volumetric flow rate, m^3/s
W	—	Power, kW
x	—	Salinity, g/kg
Z	—	Initial investment, \$
$\dot{Z}$	—	Investment rate, \$/y

Subscripts

0	—	Dead state
b	—	Brine
bf	—	Vapor flashed off from the brine
c	—	Condensing
cI	—	Condenser I
cII	—	Condenser II
cw	—	Deep cold seawater
D	—	Distillate
df	—	Produced vapor in the flashing box of distillate
e	—	Evaporator
et	—	Extraction
ex	—	Exerey efficiency
f	—	Feed water
flash	—	Distillate flashing box
g	—	Generator
hs	—	Warm seawater
i	—	Effect number of MED
in	—	Input
is	—	Isentropic
ln	—	Logarithmic mean temperature difference
mix	—	Mixer
pb	—	Brine blowdown pump
pd	—	Distillate extraction pump
pf	—	Intake seawater pump
pI	—	Pump I
pII	—	Pump II
pv	—	Vacuum pump
ref	—	Refrigeration
sw	—	Surface warm seawater
swp	—	Seawater pump
tur	—	Turbine
w	—	Working fluid

Superscripts

ch	—	Chemical

Greek

β	—	Expansion ratio
δ	—	Factor of the operating and maintenance costs
ΔP	—	Pressure difference, kPa
ΔT	—	Temperature difference, °C
η	—	Efficiency
λ	—	Latent heat, kJ/kg
μ	—	Entrainment ratio
ρ	—	Density, kg/m^3

Abbreviations

BPE	—	Boiling point elevation
CCDP	—	Combined cooling, desalination and power
CCHP	—	Combined cooling, heating and power
COP	—	Coefficient of performance
CRF	—	Capital recovery factor
ERC	—	Ejector refrigeration cycle
HDH	—	Humidification and dehumidification
MED	—	Multi-effect distillation
MSF	—	Multi-stage flash
NSGA-II	—	Non-dominated sorting genetic algorithm
ORC	—	Organic Rankine cycle
OTEC	—	Ocean thermal energy conversion
POS	—	Pareto optimal solution
PR	—	Performance ratio
RO	—	Reverse osmosis
TCR	—	Total cost rate

Acknowledgements

This research is supported by the project of National Natural Science Foundation of China (No.51936002, No.52076027), the National Key R&D Program of China (No.2019YFB1504301), and the project of the Fundamental Research Funds for the Central Universities (DUT19RC (4)040). The authors are grateful for the support.

References

[1] A. Omar, A. Nashed, Q. Li, G. Leslie, R.A. Taylor, Pathways for integrated concentrated solar power - desalination: a critical review, Renewable Sustainable Energy Rev., 119 (2020) 109609.
[2] M.A. Abdelkareem, M. El Haj Assad, E.T. Sayed, B. Soudan, Recent progress in the use of renewable energy sources to power water desalination plants, Desalination, 435 (2018) 97–113.
[3] N. Ghaffour, J. Bundschuh, H. Mahmoudi, M.F.A. Goosen, Renewable energy-driven desalination technologies: a comprehensive review on challenges and potential applications of integrated systems, Desalination, 356 (2015) 94–114.

[4] L. Ariyanfar, M. Yari, E.A. Aghdam, Proposal and performance assessment of novel combined ORC and HDD cogeneration systems, Appl. Therm. Eng., 108 (2016) 296–311.
[5] A.H. Araghi, M. Khiadani, K. Hooman, A novel vacuum discharge thermal energy combined desalination and power generation system utilizing R290/R600a, Energy, 98 (2016) 215–224.
[6] Q. Chen, R. Alrowais, M. Burhan, D. Ybyraiymkul, M.W. Shahzad, Y. Li, K.C. Ng, A self-sustainable solar desalination system using direct spray technology, Energy, 205 (2020).
[7] Q. Chen, Y. Li, K.J. Chua, On the thermodynamic analysis of a novel low-grade heat driven desalination system, Energy Convers. Manage., 128 (2016) 145–159.
[8] Q. Chen, M.K. Ja, Y. Li, K.J. Chua, Energy, exergy and economic analysis of a hybrid spray-assisted low-temperature desalination/thermal vapor compression system, Energy, 166 (2019) 871–885.
[9] M.A. Al-Weshahi, A. Anderson, G. Tian, Organic Rankine cycle recovering stage heat from MSF desalination distillate water, Appl. Energy, 130 (2014) 738–747.
[10] A. Baccioli, M. Antonelli, U. Desideri, A. Grossi, Thermodynamic and economic analysis of the integration of organic Rankine cycle and multi-effect distillation in waste-heat recovery applications, Energy, 161 (2018) 456–469.
[11] J.A. Aguilar-Jiménez, N. Velázquez, R. López-Zavala, R. Beltrán, L. Hernández-Callejo, L.A. González-Uribe, V. Alonso-Gómez, Low-temperature multiple-effect desalination/organic Rankine cycle system with a novel integration for fresh water and electrical energy production, Desalination, 477 (2020) 114269.
[12] F. Calise, M. Dentice d'Accadia, A. Macaluso, L. Vanoli, A. Piacentino, A novel solar-geothermal trigeneration system integrating water desalination: design, dynamic simulation and economic assessment, Energy, 115 (2016) 1533–1547.
[13] H. You, J. Han, Y. Liu, Performance assessment of a CCHP and multi-effect desalination system based on GT/ORC with inlet air precooling, Energy, 185 (2019) 286–298.
[14] W.F. He, F. Wu, Y.P. Kong, T. Wen, J.J. Chen, D. Han, Parametric analysis of a power-water cogeneration system based on single-extraction organic Rankine cycle, Appl. Therm. Eng., 148 (2019) 382–390.
[15] H. Uehara, Y. Ikegami, Optimization of a Closed-Cycle OTEC System, J. Sol. Energy Eng. Trans.-ASME, 112 (1990) 247–256.
[16] M. Wang, R. Jing, H.R. Zhang, C. Meng, N. Li, Y.R. Zhao, An innovative organic Rankine cycle (ORC) based ocean thermal energy conversion (OTEC) system with performance simulation and multi-objective optimization, Appl. Therm. Eng., 145 (2018) 743–754.
[17] J.-I. Yoon, C.-H. Son, S.-M. Baek, B.H. Ye, H.-J. Kim, H.-S. Lee, Performance characteristics of a high-efficiency R717 OTEC power cycle, Appl. Therm. Eng., 72 (2014) 304–308.
[18] N. Yamada, A. Hoshi, Y. Ikegami, Performance simulation of solar-boosted ocean thermal energy conversion plant, Renewable Energy, 34 (2009) 1752–1758.
[19] H. Yuan, P.L. Zhou, N. Mei, Performance analysis of a solar-assisted OTEC cycle for power generation and fishery cold storage refrigeration, Appl. Therm. Eng., 90 (2015) 809–819.
[20] H. Aydin, H.-S. Lee, H.-J. Kim, S.K. Shin, K. Park, Off-design performance analysis of a closed-cycle ocean thermal energy conversion system with solar thermal preheating and superheating, Renewable Energy, 72 (2014) 154–163.
[21] Y. Bian, J. Pan, Y. Liu, F. Zhang, Y. Yang, H. Arima, Performance analysis of a combined power and refrigeration cycle, Energy Convers. Manage., 185 (2019) 259–270.
[22] P. Ahmadi, I. Dincer, M.A. Rosen, Multi-objective optimization of a novel solar-based multigeneration energy system, Sol. Energy, 108 (2014) 576–591.
[23] S.M. Alirahmi, S. Rahmani Dabbagh, P. Ahmadi, S. Wongwises, Multi-objective design optimization of a multi-generation energy system based on geothermal and solar energy, Energy Convers. Manage., 205 (2020).
[24] H. Rostamzadeh, M. Ebadollahi, H. Ghaebi, A. Shokri, Comparative study of two novel micro-CCHP systems based on organic Rankine cycle and Kalina cycle, Energy Convers. Manage., 183 (2019) 210–229.
[25] S.H. Zhou, Y.L. Guo, X.S. Mu, S.Q. Shen, Effect of design parameters on thermodynamic losses of the heat transfer process in LT-MEE desalination plant, Desalination, 375 (2015) 40–47.
[26] S.H. Zhou, L.Y. Gong, X.Y. Liu, S.Q. Shen, Mathematical modeling and performance analysis for multi-effect evaporation/multi-effect evaporation with thermal vapor compression desalination system, Appl. Therm. Eng., 159 (2019).
[27] H. Ghaebi, T. Parikhani, H. Rostamzadeh, B. Farhang, Proposal and assessment of a novel geothermal combined cooling and power cycle based on Kalina and ejector refrigeration cycles, Appl. Therm. Eng., 130 (2018) 767–781.
[28] C.R. Upshaw, Thermodynamic and Economic Feasibility Analysis of a 20MW Ocean Thermal Energy Conversion (OTEC) Power Plant, The University of Texas at Austin, 2012.
[29] C.X. Wu, B.J. Wu, Y. Ye, A review of ocean thermal energy utilization, Adv. New Renewable Energy, 2 (2014) 454–461.
[30] W. Shi, W.M. Liu, L. Liu, J.P. Peng, F.Y. Chen, Numerical analysis on the temperature rise characteristics of seawater in vertical cold-water pipe in OTEC power plant, J. Ocean Technol., 35 (2016) 93–96.
[31] H.R. Datsgerdi, H.T. Chua, Thermo-economic analysis of low-grade heat driven multi-effect distillation based desalination processes, Desalination, 448 (2018) 36–48.
[32] B. Rahimi, A. Christ, K. Regenauer-Lieb, H.T. Chua, A novel process for low grade heat driven desalination, Desalination, 351 (2014) 202–212.
[33] Q. Chen, M.K. Ja, Y. Li, K.J. Chua, Energy, economic and environmental (3E) analysis and multi-objective optimization of a spray-assisted low-temperature desalination system, Energy, 151 (2018) 387–401.
[34] S. Zhang, The Economic Research of LT-MED and the Measures to Reduce the Cost of Product Water, North China Electric Power University, 2012.
[35] K.J. Gabriel, P. Linke, M.M. El-Halwagi, Optimization of multi-effect distillation process using a linear enthalpy model, Desalination, 365 (2015) 261–276.
[36] R.S. El-Emam, I. Dincer, Exergy and exergoeconomic analyses and optimization of geothermal organic Rankine cycle, Appl. Therm. Eng., 59 (2013) 435–444.
[37] H. Montazerinejad, P. Ahmadi, Z. Montazerinejad, Advanced exergy, exergo-economic and exrgo-environmental analyses of a solar based trigeneration energy system, Appl. Therm. Eng., 152 (2019) 666–685.
[38] M. Moghimi, M. Emadi, P. Ahmadi, H. Moghadasi, 4E analysis and multi-objective optimization of a CCHP cycle based on gas turbine and ejector refrigeration, Appl. Therm. Eng., 141 (2018) 516–530.
[39] Y.R. Li, M.T. Du, C.M. Wu, S.Y. Wu, C. Liu, J.L. Xu, Economical evaluation and optimization of subcritical organic Rankine cycle based on temperature matching analysis, Energy, 68 (2014) 238–247.
[40] C. Mata-Torres, A. Zurita, J.M. Cardemil, R.A. Escobar, Exergy cost and thermoeconomic analysis of a Rankine cycle + multi-effect distillation plant considering time-varying conditions, Energy Convers. Manage., 192 (2019) 114–132.
[41] Z.F. Wang, W. Han, N. Zhang, B.S. Su, M. Liu, H.G. Jin, Assessment of off-design performance of a combined cooling, heating and power system using exergoeconomic analysis, Energy Convers. Manage., 171 (2018) 188–195.
[42] S. Khalilzadeh, A. Hossein Nezhad, Utilization of waste heat of a high-capacity wind turbine in multi effect distillation desalination: energy, exergy and thermoeconomic analysis, Desalination, 439 (2018) 119–137.
[43] M. Esrafilian, R. Ahmadi, Energy, environmental and economic assessment of a polygeneration system of local desalination and CCHP, Desalination, 454 (2019) 20–37.
[44] F. Calise, M. Dentice d'Accadia, A. Piacentino, Exergetic and exergoeconomic analysis of a renewable polygeneration system

and viability study for small isolated communities, Energy, 92 (2015) 290–307.
[45] P. Ahmadi, I. Dincer, M.A. Rosen, Multi-objective optimization of an ocean thermal energy conversion system for hydrogen production, Int. J. Hydrogen Energy, 40 (2015) 7601–7608.
[46] M.A. Darwish, F. Al-Juwayhel, H.K. Abdulraheim, Multi-effect boiling systems from an energy viewpoint, Desalination, 194 (2006) 22–39.
[47] Y. Dai, J. Wang, L. Gao, Exergy analysis, parametric analysis and optimization for a novel combined power and ejector refrigeration cycle, Appl. Therm. Eng., 29 (2009) 1983–1990.
[48] S. Bigham, R. KouhiKamali, M.P. Zadeh, A general guide to design of falling film evaporators utilized in multi effect desalination units operating at high vapor qualities under a sub-atmospheric condition, Energy, 84 (2015) 279–288.
[49] K. Deb, A. Pratap, S. Agarwal, T. Meyarivan, A fast and elitist multiobjective genetic algorithm: NSGA-II, IEEE Trans. Evol. Comput., 6 (2002) 182–197.
[50] Y. Feng, T. Hung, Y. Zhang, B. Li, J. Yang, Y. Shi, Performance comparison of low-grade ORCs (organic Rankine cycles) using R245fa, pentane and their mixtures based on the thermoeconomic multi-objective optimization and decision makings, Energy, 93 (2015) 2018–2029.